Direct-current current transformer for the measurement of an electric propulsion ion beam

C. Volkmar,[1, a)] C. Geile,[1, b)] A. Neumann,[1, c)] and K. Hannemann[1, d)]
German Aerospace Center, Institute of Aerodynamics and Flow Technology, Spacecraft Department Bunsenstrasse 10, 37073 Goettingen, Germany

(Dated: 22 February 2019)

An important task in the development of electric propulsion devices is ground-based testing. In order to characterize electric thrusters, their generated ion beams are regarded as figures of merit and have to be well-known and understood. We present an approach to measure DC ion beam currents generated by electric thrusters by means of an inductive direct-current current transformer. In contrast to commonly used devices like Faraday cups, this device can measure the beam current non-intrusively by means of magnetic field coupling rather than charge collection. The paper shows the development of a prototype sensor which can measure currents in the typical range for electric thrusters with high resolution and satisfactorily accuracy. A detailed SPICE model to assist during hardware development is also introduced and verified by test case measurements. The prototype has been tested and validated with a radio-frequency ion thruster. Its readout shows very good agreement to the output of an analytical model which computes a Gaussian-shaped ion beam in the far-field based on experimental input data.

Keywords: Ion beam measurement, direct-current current transformer, electric propulsion

I. INTRODUCTION

The motivation of having alternative methods to measure the ion beam current generated by electric thrusters arises from the drawbacks of the current state-of-the-art methodology; i.e., intrusively accumulating charges from the beam with Faraday cups. Besides being intrusive, Faraday cups are susceptible to generate wrong readings due to secondary electrons that are emitted from the collector material by high energy ion bombardment. This issue is, however, greatly reduced by using electron repelling measures in front of the collector. Mainly due to their easy handling, Faraday cups are well established in ground-based electric propulsion facilities. More information on Faraday cups for electric propulsion testing is given in Refs. 1 and 2.

To overcome the issues associated with Faraday cups—most prominently the intrusive character—we propose a different method of acquiring the ion beam current by means of an inductive pickup sensor. In particle physics, this type of sensor is also referred to as Direct-Current Current Transformer (DCCT). The sensor is based on an arrangement of toroidal magnetic cores and can thus be installed in way that the total beam current can be measured in the near-field. Likewise, the far-field current could be monitored locally. Those two setups are depicted in Fig. 1 (a) and (b), respectively. Fortunately, the system can easily be scaled to bigger dimensions by using wider cores and more powerful supplies or a higher number of coil windings, respectively. The cores used for this work are available in different sizes, going up to several 10 cm, as suggested by Ref. 3. Even so, in the extreme far-field of a thruster, a situation as depicted in Fig. 1 (b) will be evident.

Generally, the current is averaged along its path d through the sensor according to

$$I = \frac{1}{d}\int_0^d \left(\iint_A \mathbf{J}\,\mathrm{d}\mathbf{A}\right)\mathrm{d}z, \tag{1}$$

with $\mathbf{J}$ denoting the current density, $\mathbf{A} = \mathbf{n}A$ the oriented cross section area, with $\mathbf{n}$ being the surface normal of A, and z the major axis of the sensor. Strictly under far-field conditions, some thruster outlet radii downstream of its exit plane where the ion trajectories can be assumed parallel[4], Eq. (1) simplifies to

$$I = \frac{\pi R^2}{d}\int_0^d J\,\mathrm{d}z, \tag{2}$$

with the sensor cross section area πR^2. In the near-field where the upper assumptions do not hold, the current density's radial distribution has to be taken into account and the current is given by

$$I = \frac{2\pi}{d}\int_0^d\int_0^R J\,r\,\mathrm{d}r\,\mathrm{d}z. \tag{3}$$

In the further course, the current density is evaluated on the beam axis normal to the thruster grid. Typically, current sensing mechanisms are focused on the pivot of the thruster exit but are not necessarily located on the beam axis[1].

Under far-field conditions, the variation of the current density along the major axis z is given by

$$J(z) = J_0\frac{R_0^2}{z^2}, \tag{4}$$

with the thruster outlet radius R_0 and the current density at the outlet $J_0 = I_\mathrm{b}/\pi R_0^2$, where I_b denotes the total

a) Electronic mail: chris.volkmar@dlr.de
b) Electronic mail: christopher.geile@dlr.de
c) Electronic mail: a.neumann@dlr.de
d) Electronic mail: klaus.hannemann@dlr.de

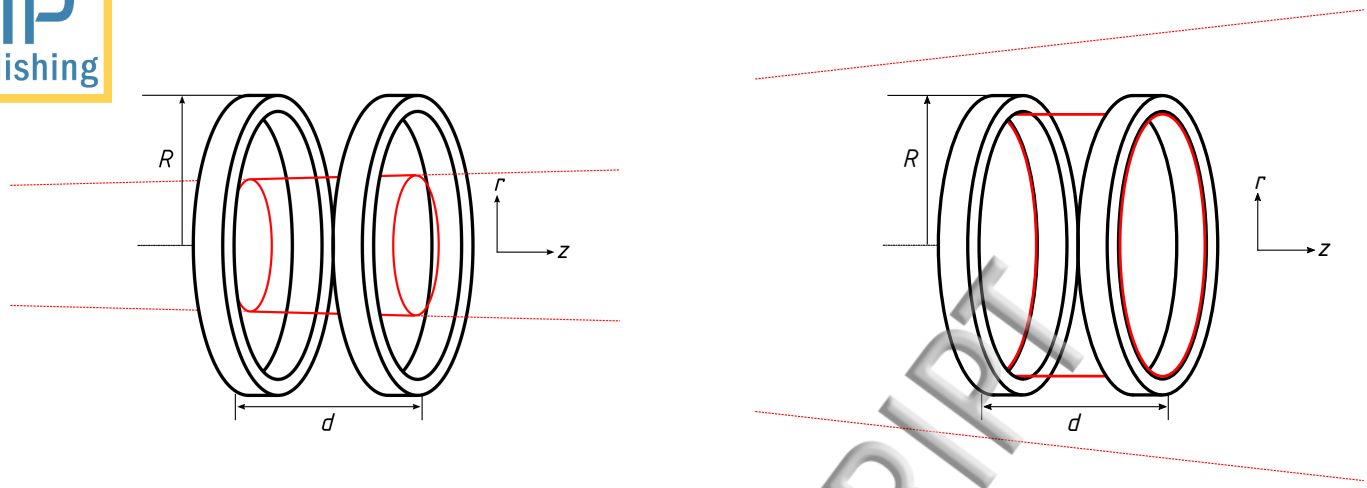

FIG. 1. a) Integral measurement of total current in the near-field. b) Local measurement of current distribution in the far-field. The effective measurement volume (solid red outline) is confined by the toroidal magnetic cores.

extracted beam current. In the far-field, where $d \ll z$ is satisfied, the influence of the axial length of the sensor is assumed negligible because $J_0 R_0^2/(z+d)^2 \approx J_0 R_0^2/z^2$.

In the upper paragraphs, the existence of electrons in the beam was neglected. This is, however, not valid for the beams produced by electric thrusters since the ion beam is neutralized by electrons. The remainder of this document will focus on a proof of principle of a pure ion beam incident to the sensor. This is a good approximation, if electron repelling measures are used to filter incoming electrons. Such measures could take the form of grids which are typically attached to Faraday cups. In a final version of the proposed sensor, an appropriate measure to deal with the beam electrons will be used for the DCCT as well. Sect. V gives a brief overview of a likely realization.

A. Direct-Current Current Transformers

The concept of DCCTs has been extensively studied by particle physicists and engineers and it has been used mainly at particle accelerators, with CERN leading the way. In the early 1980s, Unser published a pioneer work on DCCTs for ion beam measurement[5]. The idea of this research was seized by many more researchers of numerous institutions over the last decades; some of those works are shown in Refs. 6–14. Thorough overviews of the DCCT technology among other beam profiling methodologies and their application at particle accelerators, are given in Refs. 3 and 15. The DCCT methodology is based on the fluxgate magnetometer technique which has been in use for several decades; an extensive review on the subject is given in Ref. 16. Fluxgate magnetometers have commonly been used to accurately determine the Earth's magnetic field over long duration.

The DCCT technology delivers very accurate current measurements at particle accelerators due to the narrow beam width of the ion beams which is due to high kinetic energy (typically in the MeV range). With this constraint, the beam is sharply localized in the measurement device, as suggested by Fig. 1 (a). However, ion beam energies in electric thrusters are some orders of magnitude smaller (typically in the single-digit keV range) and thus, those beams are considerably broader because space charge effects are more pronounced. That could lead to unintended heating of the sensor due to particle fluxes to its structure. Additionally, the effect of secondary electrons, which may be set free by ion bombardment of the sensor's inner channel surface, could lead to wrong readouts. Although, due to short channel length and narrow angles of incident ions with respect to the channel surface, this effect is believed to be of minor importance. Still, it might be necessary to design appropriate countermeasures which compensate for those upper mentioned effects.

The fundamental functionality of DCCTs is given by the nonlinear magnetization of ferromagnetic materials. This otherwise unwanted phenomenon is used for DC current determination. A DCCT is constituted by two magnetic cores that are magnetized by a modulation signal; in this case either a sine or a square wave. As shown in Fig. 2, the modulation windings are reversed in order to achieve a phase shift of π between the two windings wrapped around the respective cores. The modulation signal amplitude and the number of windings are chosen to sufficiently saturate the cores. The magnetic fluxes in the respective cores also show a phase shift of π, leading to minimum induced voltage across the sense winding which is wrapped around both cores in a straight way. The net induced voltage would ideally become zero if the magnetic circuits (constituted by the cores and windings) would be identical. However, in reality small variations of the cores' characteristics (permeability in the linear operation mode, temperature effects, etc.) lead to a mismatch that causes the induced voltage being greater than zero. If a DC (beam) current offsets both cores simultaneously, the magnetic hystereses of both cores are shifted towards

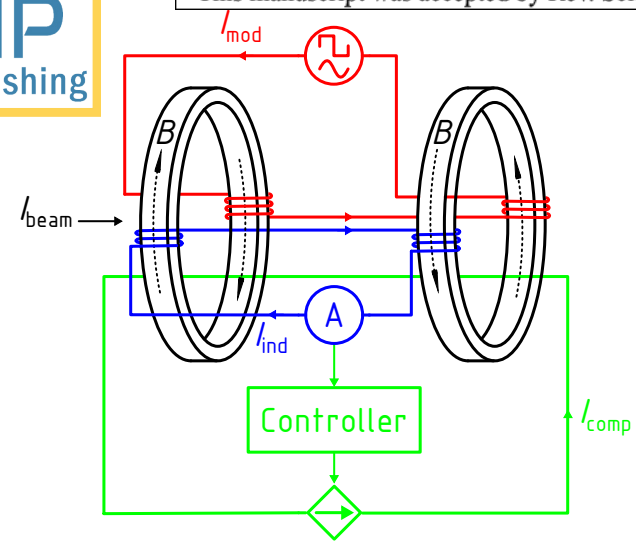

FIG. 2. Conceptual design of a DCCT (reproduced from P. Forck, Lecture Notes on Beam Instrumentation and Diagnostics, Gesellschaft fr Schwerionenforschung (GSI), Joint University Accelerator School (Darmstadt, Germany, 2011), Copyright 2011 P. Forck). The red circuit indicates the modulation branch with the modulation current I_{mod}, the blue circuit corresponds to the sensing branch. The positive ion beam is compensated by the compensation current I_{comp} shown in the green branch. The compensation current is generated as a function of the induced current I_{ind} in the sensing branch and is controlled with a microcontroller.

the positive or negative saturation limits, depending on the phase of the modulation signal. Thus, the magnetic fluxes do not cancel each other exactly and an induced voltage is observable across the sense windings.

The series circuit of sense windings can be changed to a parallel one, with a symmetric common ground to both windings. In a parallel setting, a differential amplifier can be used to measure the net induced voltage without loading the coils. Whatever representation is chosen, the net induced voltage waveform shows a fairly high bandwidth due to nonlinear effects caused by the magnetic hystereses. In this work, with fundamental frequency of 5 kHz we found harmonics ranging to several hundred kHz with sine excitation and several MHz with square wave excitation. Since the second harmonic shows the strongest spectral peak[9], which is caused by two saturation area transitions per period, an electrical filter is commonly used to suppress higher harmonics and thus increase SNR (signal-to-noise-ratio).

The induced voltage is the figure of merit for the demodulator, which is in turn used to generate a set point value for the controller which triggers a compensation current that is driven through both cores to balance the beam current. The compensation current is, therefore, a measure for the beam current:

$$I_{\mathrm{b}} = I_{\mathrm{comp}} \pm \Delta I \tag{5}$$

The error ΔI is mainly caused by mismatch of the cores but also by the noise level of the electrical circuitry. It can be decreased by calibration of the system and adequate filtering of the induced signal.

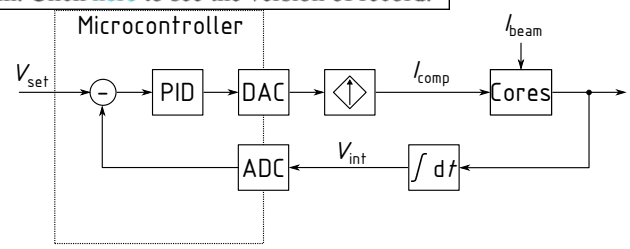

FIG. 3. Overview of the system in closed-loop mode. The integrator voltage V_{int} is proportional the the beam current I_{b} and is used as the controlled variable. It is compared to a set point value V_{set} and then controlled by a PID controller which digitally triggers the compensation current I_{comp}.

Figure 3 gives an overview of the proposed DCCT, consisting of the modulator stage, demodulator/integrator stage, actuator for the compensation current, and a microcontroller.

II. DESIGN OF THE DCCT

The in-house DCCT should be used with a variety of electric thrusters, hence it should cover a high measurement range. Here, we aspire a working range from 10 µA – 10 mA; i.e., 4 orders of magnitude.

The circuit diagram of the proposed sensor is shown in Fig. 4. The op-amps used exhibit low-noise and high gain-bandwidth product.

As described above, the secondary transformer windings are symmetrical to ground which results in the need of taking a difference rather than a sum of the induced voltages. Here, a differential amplifier is used to demodulate the high bandwidth burst signal which is induced at the transformer secondary. The advantage of using a differential amplifier is that the transformer is not loaded as the op-amp's input impedance is very high. Additionally, filtering for the second harmonic is performed directly at the differential amplifier. Here, the bandwidth of the resulting signal is filtered with a symmetrical low-pass filter to significantly reduce emc related issues.

The most important parts of the sensor are, of course, the magnetic cores used for the nonlinear signal generation. It is crucial that the magnetic characteristics of the cores used are very similar; exact at best. Prior to assembly, all available cores were characterized using a test circuit shown in Fig. 5 to determine the correlation of the $B-H$ curves of the cores. Under consideration of Ampre's and Faraday's laws, the magnetic field H and magnetic induction B can be derived as functions of the circuit elements (in this case for toroidal magnetic cores):

$$H(t) = \frac{N_1}{l_{\mathrm{m}} R_1} v_{R_1}(t) \tag{6}$$

$$B(t) = -\frac{R_2 C}{N_2 A_{\mathrm{Fe}}} v_C(t) \tag{7}$$

In these equations, N_1 and N_2 denote the transformer's number of primary and secondary windings, respectively, l_{m} the mean length for magnetic field lines inside the toroidal core with rectangular cross section, and A_{Fe} the

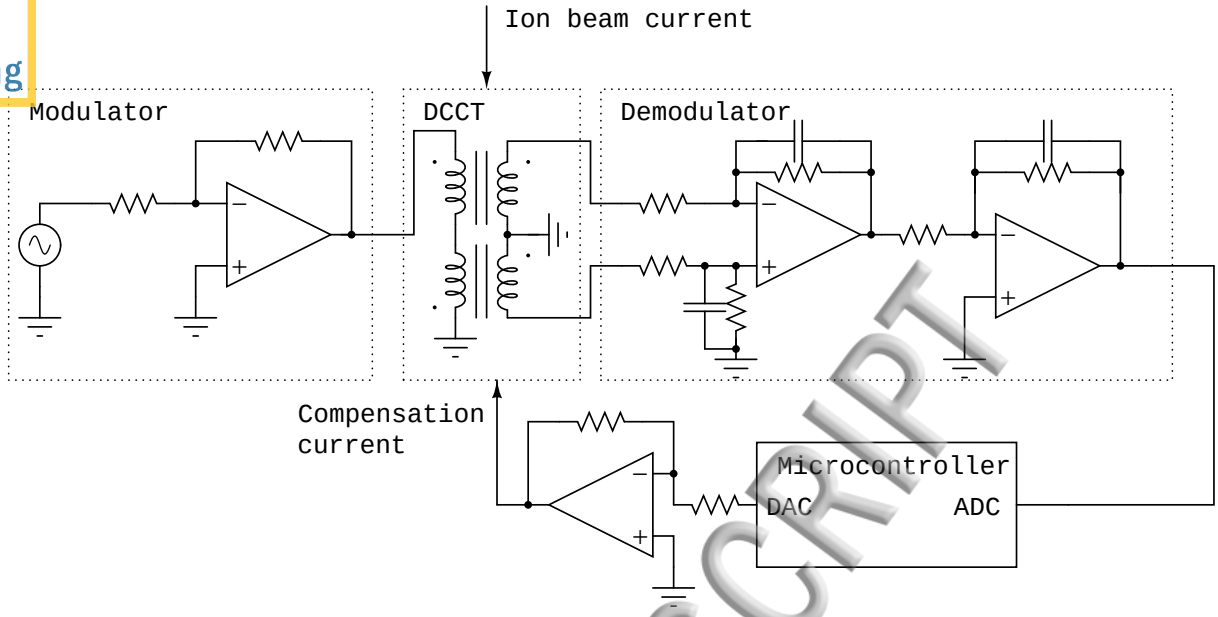

FIG. 4. Simplified circuit diagram of the proposed sensor system. This diagram is furthermore the base for a more complex SPICE model, which will be discussed in Sect. III.

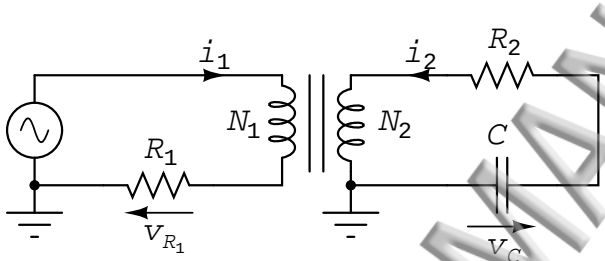

FIG. 5. Circuit diagram used to characterize the magnetic characteristics of the used cores. With this circuit, the $B-H$ curve can be obtained.

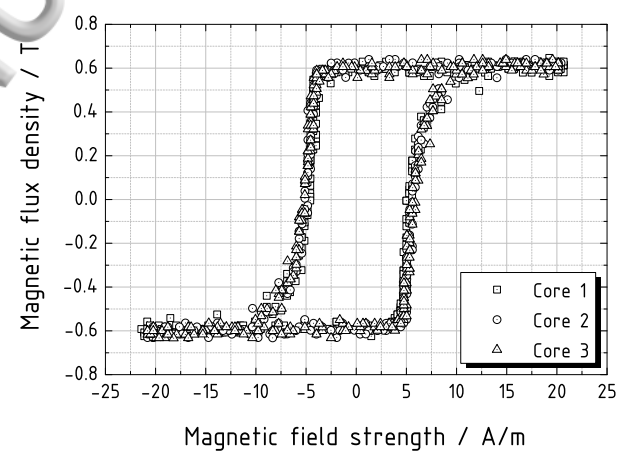

FIG. 6. $B-H$ curves of three different cores. The curves are correlated almost perfectly.

area the magnetic field lines pass through. Those values can be obtained by measurement or taken from data sheets. The voltages are acquired with an oscilloscope in x/y mode, offering direct visualization of the hysteresis.

The obtained $B-H$ curves of three different cores of type VITROVAC 6025 Z, manufactured by Vacuumschmelze GmbH, Germany, are shown in Fig. 6. As can be seen, they are correlated well enough to not load the modulation stage asymmetrically. Evidently, the cores offer extremely low coercivity, around $5\,\mathrm{A\,m^{-1}}$, and fairly high saturation flux density ($\approx 0.6\,\mathrm{T}$). This leads to high permeability in linear mode and low driving current which facilitates the choice of components as well as thermal management considerably. Those characteristics are enabled by amorphous Co-based nanocrystalline ferromagnetic stacked strips and a corresponding specialized manufacturing process, resulting in a soft-magnetic alloy with rectangular hysteresis loop. More information can be found in a technical note from the manufacturer[17].

The loop is closed via a feedback current through the cores, in opposite direction to the (positive) ion beam current. When the magnetic cores exhibit net magnetic flux due to DC beam current, the induced voltage is integrated with a small time constant. The integrated stable voltage V_{int} is converted to a digital signal by a 12 bit analog-digital-converter (ADC). The microcontroller then compares this value, which is proportional to the net magnetic flux through both cores, with a set point voltage V_{set}, which is typically around but not exactly 0 V to account for biasing effects which occur at the PCB layer. The set point voltage can be set to any value up to 3.3 V. The difference of the signals is fed to a proportional-integral-differential (PID) controller which outputs a digital compensation signal. This signal is transformed to an analog voltage V_{DAC} within a 12 bit digital-analog-converter (DAC). The analog voltage is used to trigger the actuator stage. The actuator is basically a switchable current source based on a low noise, high speed operational amplifier and a shunt resis-

tor R. The compensation current is thus given by:

$$I_{\mathrm{comp}} = \frac{V_{\mathrm{DAC}}}{R} \tag{8}$$

The PID controlling scheme is implemented digitally and needs the controller gains as inputs. Those gains can be passed to the program using a serial interface and a LabView™ GUI. The controller algorithm is implemented in parallel form and fully recursively to inhibit the wind-up effect caused by the integral part and to generally enhance control performance[18]. The integration is performed using the trapezoidal rule and the differentiation is approximated by the backward Euler method. The careful choice of the absolute gain values is shown in Sect. II A. With the discrete time $t\,[kT_{\mathrm{s}}] = t^k$, where T_{s} denotes the sampling time, the controller algorithm reads:

$$\begin{aligned} V_{\mathrm{DAC}}^{k} = V_{\mathrm{DAC}}^{k-1} &+ \left(K_{\mathrm{p}} + \frac{K_{\mathrm{i}}T_{\mathrm{s}}}{2} + \frac{K_{\mathrm{d}}}{T_{\mathrm{s}}}\right) e^{k} \\ &- \left(K_{\mathrm{p}} + 2\frac{K_{\mathrm{d}}}{T_{\mathrm{s}}} - \frac{K_{\mathrm{i}}T_{\mathrm{s}}}{2}\right) e^{k-1} + \frac{K_{\mathrm{d}}}{T_{\mathrm{s}}} e^{k-2} \end{aligned} \tag{9}$$

Here, K_{p}, K_{i}, and K_{d} denote proportional, integral, and differential gains, respectively, and $e^k = V_{\mathrm{set}} - V_{\mathrm{int}}^k$ denotes the error at discrete time t^k. The recursive form can be derived from the Laplace transform of the controller transfer function and by substituting occurring differentials by their respective difference quotients again following the backward (implicit) Euler method[19].

A. System Identification and Controller Settings

Before the SPICE model is presented in Sect. III, a system identification and, based on that, the derivation of optimal control parameters are presented because the sensor has been simulated in closed-loop mode.

The system behavior was identified by evaluating the open-loop step response of the controlled variable V_{int}. With the actuator voltage V_{DAC} a digitally controlled current source is formed following Eq. (8) to generate the 1 mA step. In closed-loop mode, this branch is used to set the compensation current. The data logging of the sensor was sampled with $T_{\mathrm{s}} = 5\,\mathrm{ms}$ and triggered by the step, hence causal coherence is satisfied. The step response of the open-loop system is shown in Fig. 7.

The step response has been fitted by a standard first order exponential decay function of form $y(t) = y_0 + A\exp(-t/\tau)$, with coefficient of determination of $R^2 = 0.99314$. Thus, the plant is very accurately approximated by a first order lag element with $A = K_0$ and $y_0 = 0$. The corresponding transfer function in the s domain reads:

$$G(s) = \frac{K_0}{T_1 s + 1} \tag{10}$$

The open-loop gain K_0 is found by following the response until it has stabilized, resulting in $K_0 = 0.19908$. With the time constant τ of a decaying exponential, the time

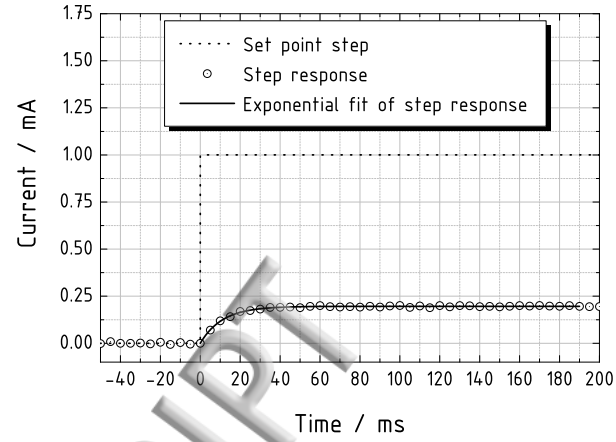

FIG. 7. 1 mA step response of the system in open-loop mode. The measured data is fitted by a first order exponential function with $R^2 = 0.99314$.

constant of the system T_1 is obtained by setting $t = T_1 = \tau$ and plugging it in the exponential form:

$$1 - \exp\left(-\frac{T_1}{\tau}\right) = 1 - \exp(-1) = 0.632 \tag{11}$$

In other words, the time constant is given by $h(T_1) = 0.632\,h(\infty) = 0.632\,K_0$, with the step response being the inverse Laplace transform of the plant transfer function times the transfer function of the unit step $1/s$; i.e., $h(t) = \mathcal{L}^{-1}\{G(s)/s\}$. Following this procedure, the time constant is found to be $T_1 = 11.6\,\mathrm{ms}$.

After the system has been identified and all the relevant parameters to describe the plant have been found, the controller gains could be found empirically with help of an automated model. The constraints of the algorithm to find the gains are a) high control performance; i.e., minimum settling time, and b) negligible steady-state error $\lim_{t\to\infty} e = 0$. With this configuration, the controlling scheme shown in Eq. (9) essentially reduces to a proportional-integral one, resulting in dropping of all the K_{d} terms.

The behavior of the controlled signal in closed-loop mode is shown in Fig. 8, with gains $K_{\mathrm{p}} = 0.06$ and $K_{\mathrm{i}} = 14.23$ (and $K_{\mathrm{d}} = 0$), as suggested by the empirical model mentioned in the last paragraph.

As can be seen in the figure, the controller permits an overshoot of approx. 10 %, resulting in high control performance. Furthermore, there is no observable steady-state error as long as $I_{\mathrm{b}} \gg 10\,\mu\mathrm{A}$. There will be more information on that subject in the next section.

III. SPICE SIMULATION

This section shows some details of the SPICE model which has been used to assist during hardware development and to validate the controller settings. The simulated circuit is based on the one shown in Fig. 4. The SPICE circuit consists mainly of the upper mentioned modular functions; i.e., modulator, nonlinear

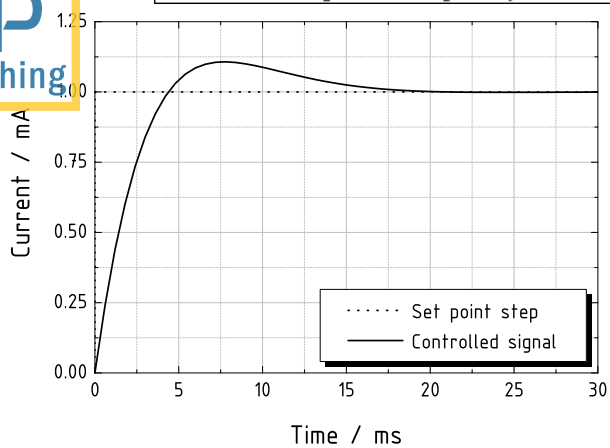

FIG. 8. Closed-loop behavior of the compensation current with $K_\mathrm{p} = 0.06$, $K_\mathrm{i} = 14.23$, and $K_\mathrm{d} = 0$.

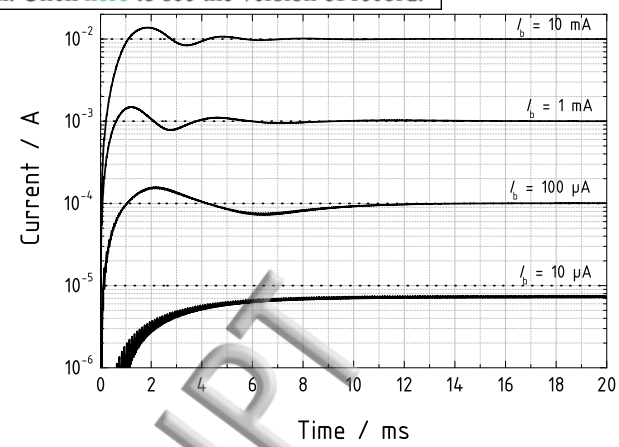

FIG. 9. Dynamic range and accuracy of the proposed DCCT. In the 10 µA range, an error of roughly 3 µA is predicted by the model.

transformer, demodulator, and the feedback system including the controller. For the simulations, libraries of the actual operational amplifiers used in the hardware version have been compiled and parameterized. Furthermore, a nonlinear inductor model introduced by Chan in Ref. 20 has been incorporated into the transformer model in order to correctly account for hysteresis effects. The important thing is to take the mutual interconnection of primary (modulator) and secondary (demodulator) circuit into account. This implies that the driving voltage at the DCCT induces magnetic flux with several harmonics, depending on the input current. This does not only have an effect on the induced voltage but also on the driving voltage itself, making it a self-consistent problem according to the transformer equation[21]:

$$\begin{pmatrix} v_1 \\ v_2 \end{pmatrix} = \begin{pmatrix} L_1 & M \\ M & L_2 \end{pmatrix} \begin{pmatrix} \dot{i}_1 \\ \dot{i}_2 \end{pmatrix} \tag{12}$$

In this equation, v_1 and v_2 denote the voltages at the primary coil with inductance L_1 and the secondary coil with inductance L_2, respectively. Furthermore, M denotes the mutual inductance $M = \zeta\sqrt{L_1 L_2}$, with coupling coefficient ζ, which is assumed to be near unity due to high permeability of the magnetic cores. Additionally, $\dot{i} = \mathrm{d}i/\mathrm{d}t$.

The Chan model takes the mutual coupling thoroughly into account which will be shown in Sect. III A.

The transformer model is parameterized with the earlier obtained values from the hysteresis loop of the magnetic cores; i.e., coercivity H_c (the intersection of the major loop of the hysteresis curve with the positive H axis), remnant flux density B_r (the intersection of the major loop with the positive B axis), and the saturation flux density B_s (the limit of the magnetic flux density according to $\lim_{H\to\infty} B \approx \mu_0 H + B_\mathrm{s}$).

The SPICE analysis has been used to determine the necessary amplification factors, protective circuits, filtering stages, etc. Furthermore, the performance of the system in closed-loop mode and its accuracy are evaluated by the model. The latter is shown in Fig. 9.

The range of operation is shown in the figure. As can be seen, roughly four orders of magnitude, ranging from 10 µA to 10 mA, of beam current can be measured with the DCCT. The model predicts stable and accurate operation of the sensor down to some 10 µA. However, going to even lower currents, the sensor exhibits a non-negligible error caused by offsets in the op-amps and imbalances of the magnetic cores used. The model is capable of reflecting this sophisticated level of accuracy because all its components have been parameterized by measured values or, in the case of the op-amps used, by data sheet entries.

A. Model Validation

The SPICE model has been validated before it has been used to assist during hardware development. The most crucial and complex part of the model is comprised by the nonlinear transformer model as mentioned in the last section. Therefore, the validation was chosen carefully to specifically show the correct behavior of this crucial part. Figure 10 shows the simulated and measured voltage at the transformer primary, with a purely sinusoidal excitation signal.

As can be seen in the figure, simulation and experiment agree extremely well. Higher harmonics, which occur due to the nonlinear effects of the magnetic cores and are coupled back to the primary circuit by the mutual inductance; i.e., $v_1 = \mathrm{j}\omega\,(i_1 L_1 + i_2 M)$, which directly follows from Eq. (12), with $\mathrm{j}\omega = \mathrm{d}/\mathrm{d}t$, are correctly taken into account by the Chan model. Both, simulation and experiment used a sine voltage with 5 kHz driving frequency.

IV. EXPERIMENTAL RESULTS

This section shows the experimental results obtained by the proposed sensor. First, a proof of principle under laboratory conditions is shown in Sect. IV A, followed by a test *in vacuo* with an electric radio-frequency (RF) ion thruster in Sect. IV B.

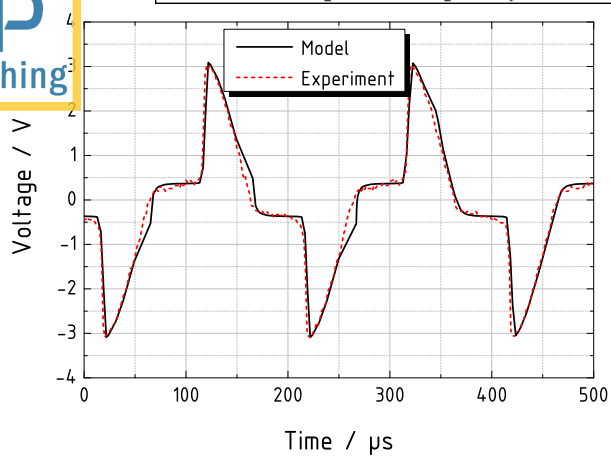

FIG. 10. Validation of the SPICE model. The voltage at the transformer primary is shown. Due to nonlinear effects caused by the magnetic hysteresis, the driving sinusoidal signal gets distorted by higher harmonics. The agreement of simulation and experiment is nearly perfect which gives credit to the Chan model used.

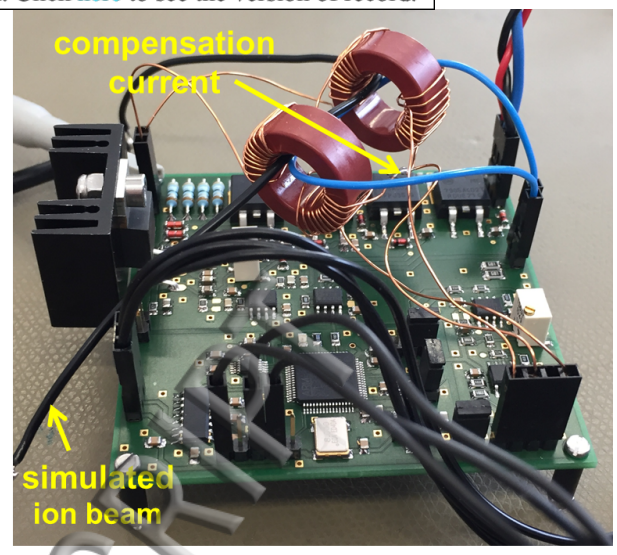

FIG. 11. DCCT hardware with the sensor board. A current-carrying wire is used to simulate the ion beam for the proof of principle. The compensation current is oriented in opposite direction to the simulated ion beam current.

A. Proof of Principle

To proof the principle function of the DCCT, a wire-bound current is fed through the sensor, as shown in Fig. 11. As can be seen, the actual sensor, comprised of the two magnetic cores, is here attached near to the circuit board. However, due to low driving frequency, the cable length could exceed at least a few meters which has been tested successfully. Furthermore, the cores are not shielded in this setup. It was found out that shielding against electromagnetic interference is not of major importance, because only current passing through the aperture of the sensor will cause a measurable effect. However, in the final version the wires of each coil are twisted to lessen magnetic interference and shielded to suppress capacitive coupling which could both occur due to their lengths.

The simulated ion beam was generated by a calibrated µA current source which was manually switched on and off. The measured values can be seen in Fig. 12, together with the absolute values of current drawn from the source. The current going through the cores adds to a certain level of bias current, inherent to the PCB layout with all of its components, linearly. Thus, a simple difference is taken to obtain the correct value; this procedure is here referred to as Δ measurement.

As can be seen in the figure, the bias level shifts slightly upwards with increasing time. That effect is believed to be caused by thermal effects. It will be assessed in more detail in Sect. IV B.

The error of the sensor, which can be evaluated from the data of Fig. 12, is depicted in Fig. 13.

The error lies in the single percentage area down to several hundred µA. Going to even lower currents, the error increases to roughly 25 % in the vicinity of 50 µA. Given the resolution of the sensor in its current version; i.e., 2.37 µA, the error lies within this order of magnitude which limits the sensor's capabilities for even lower currents. The increasing error is based on the SNR which decreases with decreasing current to be measured due to biasing effects of the electronic components used. Furthermore, the Barkhausen effect, which can be understood as magnetic noise, leads to an intrinsic mismatch of the cores used[22]. This effect is less pronounced when the cores are saturated strongly; i.e., when higher currents are measured—and vice versa.

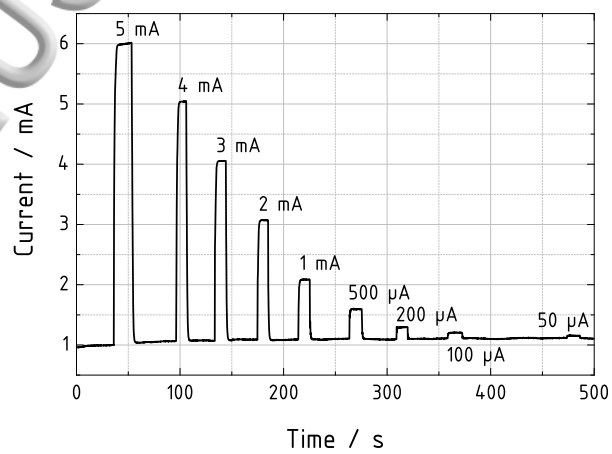

FIG. 12. Measurement results of the sensor in laboratory setup. The current was stepped from 5 mA down to 50 µA. The measured current has to be corrected by subtracting the bias current prior to or after a measurement; this procedure is called Δ measurement. A slight increase of the bias level is observable.

B. Test with RF Ion Thruster RIT-10/37

To proof the correct functionality of the proposed DCCT with an electric thruster, the sensing cores have been installed within a vacuum chamber, decoupled from

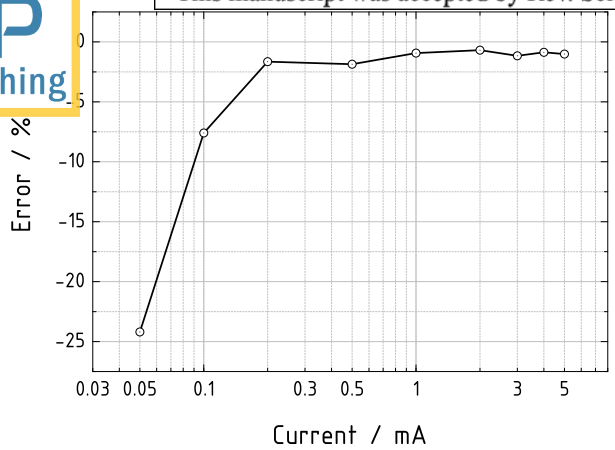

FIG. 13. Relative error of the sensor. The error increases with decreasing current, attributed to the bias currents which lie in the area of several µA as well as imbalances of the magnetic cores.

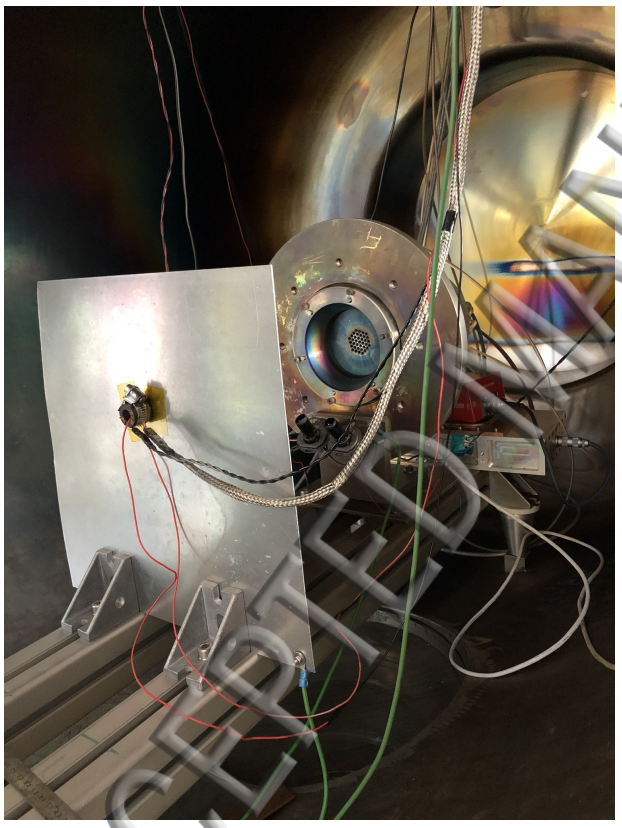

FIG. 14. DCCT prototype installed in a vacuum chamber. The remainder of the extracted ion beam, which is not measured by the DCCT, is collected in the plane of the sensor by an aluminum plate and shorted to ground. This procedure is merely a safety measure to prevent the sensor and cables from overheating or being destroyed by ion sputtering.

the electronics, in contrast to the setup in Fig. 11. The electronics could be placed outside the vacuum chamber due to low driving frequency (which facilitates longer cables). The setup is shown in Fig. 14.

The aluminum plate was used to prevent the sensor and its cables from overheating. There is a small orifice having the same diameter as the magnetic cores to cut off all the particles beyond this region. Following this procedure, a situation shown in Fig. 1 (a) is constructed, with $r = R$. In a future version, a housing will fixate the sensor and the cables to shield them against incident ions and prevent the system from overheating.

A radio-frequency ion thruster (RIT) with 10 cm diameter plasma chamber and 37 extraction apertures, called RIT-10/37, has been used for the test of the sensor. The thruster has been mounted 20 cm away from the sensor in axial z direction. Due to the fact that only a small fraction of the extraction grid is used to expel ions, with the effective extraction radius R_{eff}, a far-field situation after Ref. 4 is created with $z/R_{\mathrm{eff}} = 6.7$. Given this condition, Eq. (4) holds true.

The operating conditions of the xenon-driven thruster are summarized in Tab. I.

The measured current signal is shown in Fig. 15 and extracted from that, by evaluating each Δ, Tab. II lists the actual captured beam currents. Evidently, the first "beam off" event shows a glitch, most likely caused by insufficient duration between this event and the following "beam on" event. Therefore, this value is discarded from further evaluation.

TABLE I. Overview of the operating conditions of the RF ion thruster RIT-10/37 for the test of the DCCT. Xenon has been used as propellant.

$\dot{m}$ / sccm	V_{scr} / V	V_{acc} / V	P_{RF} / W	P_{DC} / W	I_{b} / mA
1	1,800	−300	22.7	45.6	12.6

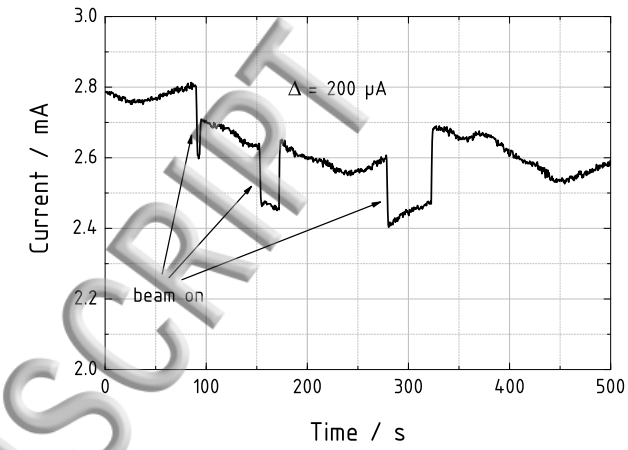

FIG. 15. Measured current for the *in vacuo* experiment with the RIT-10/37. The ion beam current through the sensor is evaluated by a Δ measurement. The bias level oscillates slightly due to thermal effects and magnetic noise.

TABLE II. Δ measurement results. Each "beam on" and "beam off" event shown in Fig. 15 is evaluated.

	Event 1	Event 2	Event 3
Beam On:	208.56 µA	177.75 µA	203.82 µA
Beam Off:	111.39 µA	196.71 µA	213.30 µA

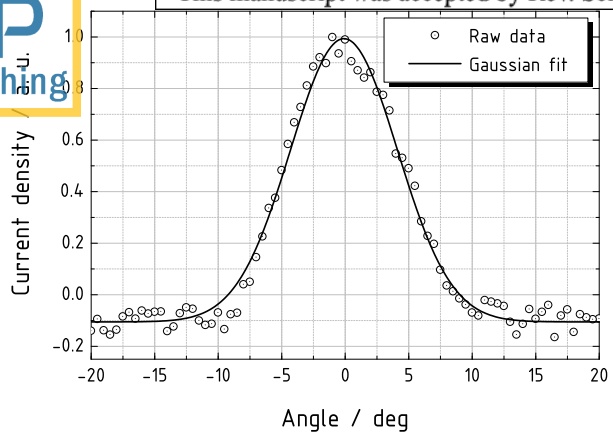

FIG. 16. Measured current profile of the RIT-10/37 with Gaussian fit. The divergence angle is about 8°. The data has been obtained in the extreme far-field with $z/R_{\text{eff}} = 23.5$ but is still considered to be representative for the arrangement depicted in Fig. 14. The offset is due to electronic noise.

In the configuration from Tab. I, the thruster exhibits an extremely low divergence angle of roughly 8° (cf. Fig. 16). The characteristics of this thruster are very well known from simulations[23,24] and experimental observations; the far-field current density distribution follows a symmetrical 2D Gaussian shape[25,26] (the sensor sits at $r = 0$):

$$J(r,z) = \frac{I_\text{b}}{2\pi\sigma^2(z)} \exp\left(-\frac{r^2}{2\sigma^2(z)}\right) \tag{13}$$

The double divergence angle is here defined as to contain 95 % of the total beam current which is common in the electric propulsion community. For a symmetrical 2D Gaussian distribution, this results in a standard deviation of 2.4477σ; i.e., $0.95 I_\text{b}$ is contained within $\pm 2.4477\sigma$ of the distribution. Figure 16 shows a measured profile, typical for the thruster used in this work.

Under far-field conditions, the current density is approximated by a plane wave; i.e., the standard deviation can be evaluated as a function of the axial distance z and the divergence angle α by a simple trigonometric relation:

$$\sigma = \frac{z}{2.4477} \tan\alpha \tag{14}$$

To evaluate the current obtained by the proposed DCCT, Eqs. (13) and (14) are used to build up a model which corresponds to the setup shown in Fig. 14. The model computes the current density at the sensor plane, using the thruster parameters shown in Tab. I as well as a divergence angle of 8°—which has been verified in Fig. 16—as input parameters. After computing the current density at the sensor plane, an interpolation over the actual sensor orifice is performed, with an orifice of $d = 1\,\text{cm}$ diameter, to obtain the collected sensor current I_s. Since the sensor is situated in the far-field and due to negligibly small axial thickness, no variation of the current density along the sensor axis is assumed. With this, the current is obtained by a simplified version of Eq. (2):

$$I_\text{s} = 2\pi \int_0^{\frac{d}{2}} J\, r\, \mathrm{d}r \tag{15}$$

The computation yields a result of $I_\text{s} = 197.78\,\mu\text{A}$ which agrees nicely and conclusively with the measured values shown in Fig. 15 and Tab. II. Assuming the computed value correct, the mean error of the sensor values from Tab. II (disregarding the outlier) is 5.4 %. Despite the sign this value agrees well with the findings from Fig. 13.

V. CONCLUSION

We have presented an alternative approach to measure ion beam currents generated by electric thrusters. The DCCT methodology has been extensively used at particle accelerators in the last decades, so it is believed that the benefits of this method should be applied to electric propulsion facilities as well. The advantages of the system have been worked out in the course of the paper and should be listed here briefly again: robustness, scalability, and accuracy. Additionally, it is believed that a combination of Faraday cups and the proposed type of sensor may get rid of issues with unknown transmission of the cups which ultimately leads to wrong current readouts. A DCCT might be placed right in front of a Faraday cup to have an *in situ* method to evaluate the integral transparency function of the Faraday cup.

The challenge of making a DCCT suitable for electric propulsion purposes lies in the low energies typically used for those thrusters. This and the fact that the current is typically collected in the far-field—which leads to very low local current density—still is regarded as very cumbersome to handle.

We have shown the principle functionality of an in-house DCCT for electric propulsion testing and we have disclosed the complete development process, consisting of both hardware and software analyses. However, there are still some open points to address in order to make the sensor better suited for continuous operation. Especially the thermal management has to be optimized; e.g. by designing an appropriate housing which may also shield against electromagnetic radiation (emission and immission). Furthermore, the sensor has yet to be tested with a neutralized ion beam. However, a basic electron repelling ring could be used as a filter in front of the sensor orifice. This would not lessen the transmission of ions while beam electrons could be suppressed to a great extent.

The most important work to be done is to reduce the error in the low-current range which is right now about 25 % for currents in the double-digit µA range. It is believed, and suggested by literature, that the driving electronics exhibit offsets and bias currents that limit accuracy for lower currents. This will be addressed by a hardware redesign of the PCB and by re-evaluating the components used. Additionally, the mismatch of the magnetic cores cause an inherent error. This effect can be addressed by either generating a bigger database of correlation between certain cores or by actively compensating those mismatches using elaborate circuitry.

Currently, an automated procedure to evaluate the Δ values online is implemented. Those have, so far, been obtained by manual evaluation of the data. Those values are supposed to show on a display attached to the sensor

(or in the LabView™ software).

We hope that other research groups will catch up on this work and we believe that the DCCT technology can ultimately be used to overcome the issues associated with Faraday cups.

[1] D. Brown *et al.*, *J. Propul. Power* **33**, 582 (2017).
[2] C. Bundesmann *et al.*, *Eur. Phys. J. D* **70**, 212 (2016).
[3] P. Forck, "Lecture Notes on Beam Instrumentation and Diagnostics–Joint University Accelerator School," Tech. Rep. (Gesellschaft fuer Schwerionenforschung (GSI) Darmstadt, 2011).
[4] T. W. Reynolds, "Mathematical Representation of Current Density Profiles from Ion Thrusters," Tech. Rep. NASA TN-D6334 (NASA Lewis Research Center, 1971).
[5] K. Unser, *IEEE Trans. Nucl. Sci.* **NS-28**, 2344 (1981).
[6] D. Bělohrad, *Fast Beam Intensity Measurements for the LHC*, Ph.D. thesis, Czech Technical University in Prague (2010).
[7] L. Callegaro, C. Cassiago, and E. Gasparotto, *IEEE Trans. Instrum. Meas.* **64**, 723 (2015).
[8] K. Knaack and M. Lomperski, in *Proceedings of the 2nd meeting in the framework of the CARE-HHH-ABI networking, DC current transformers and beam-lifetime evaluations* (2004).
[9] S. Nair, A. Cheeran, V. Teotia, and S. Malhotra, *IJERT* **4**, 1349 (2015).
[10] E. Soliman *et al.*, in *Proceedings of the 3rd International Beam Instrumentation Conference (IBIC 2014)* (2014).
[11] Z. Zhao *et al.*, *IEEE Trans. Appl. Supercond.* **20**, 1131 (2010).
[12] P. Odier, M. Ludwig, and S. Thoulet, in *Proceedings of the 9th European Workshop on Beam Diagnostics and Instrumentation for Particle Accelerators (DIPAC 2009)* (2009).
[13] U. Raich, in *Proceedings of the 2nd meeting in the framework of the CARE-HHH-ABI networking, DC current transformers and beam-lifetime evaluations* (2004).
[14] H. Reeg, in *Proceedings of the 2nd meeting in the framework of the CARE-HHH-ABI networking, DC current transformers and beam-lifetime evaluations* (2004).
[15] P. Odier, in *Proceedings of the 2nd meeting in the framework of the CARE-HHH-ABI networking, DC current transformers and beam-lifetime evaluations* (2004).
[16] F. Primdahl, *J. Phys. E: Sci. Instrum.* **12**, 241 (1979).
[17] Vacuumschmelze GmbH, "Pk-002: Tape-Wound Cores for Magnetic Amplifier Chokes," Tech. Rep. (1998).
[18] K. J. Åstrm and T. Hgglund, *Advanced PID Control* (ISA–The Instrumentations, Systems, and Automation Society, 2006).
[19] R. Isermann, *Digital Control Systems - Volume I: Fundamentals, Deterministic Control* (Springer, 1989).
[20] J. H. Chan *et al.*, *IEEE TCAD* **10**, 476 (1991).
[21] J. D. Jackson, *Classical Electrodynamics*, 3rd ed. (Wiley, 1998).
[22] J. L. M. J. van Bree, J. A. Poulis, and F. N. Hooge, *Appl. Sci. Res.* **29**, 59 (1974).
[23] C. Volkmar and U. Ricklefs, *Eur. Phys. J. D* **69**, 227 (2015).
[24] C. Volkmar, C. Geile, and K. Hannemann, *J. Propul. Power* **34**, 1061 (2018).
[25] I. S. Gilmore and M. P. Seah, *Surf. Interface Anal.* **23**, 248 (1995).
[26] C. E. Sosolik *et al.*, *Rev. Sci. Instrum.* **71**, 3326 (2000).

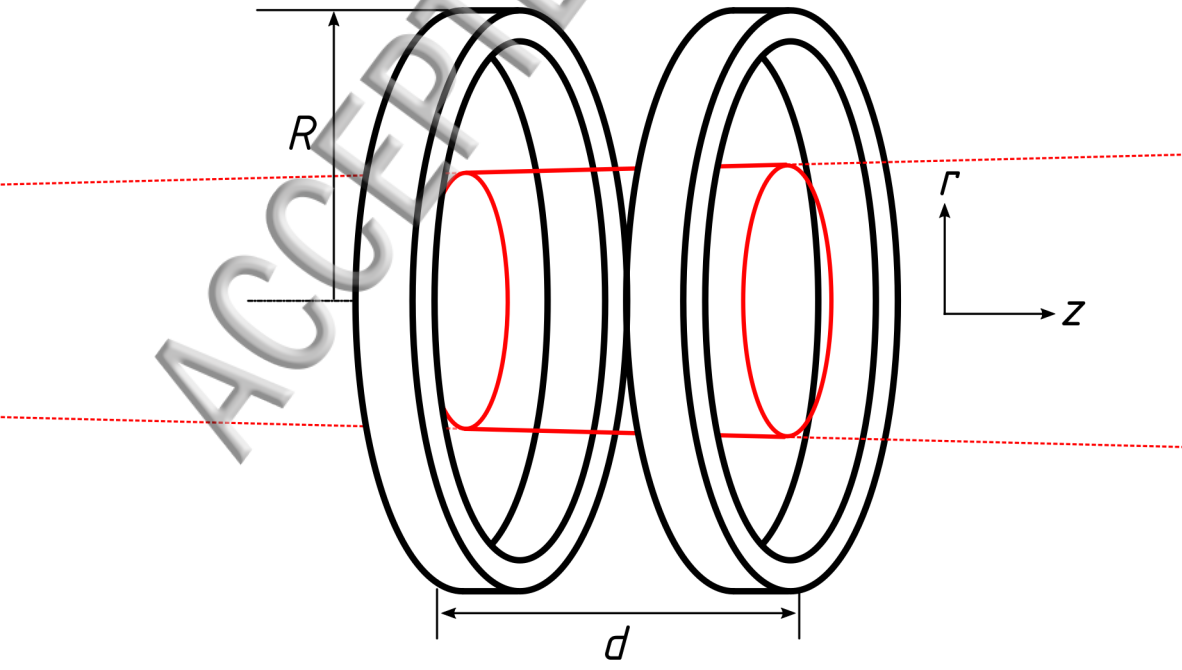

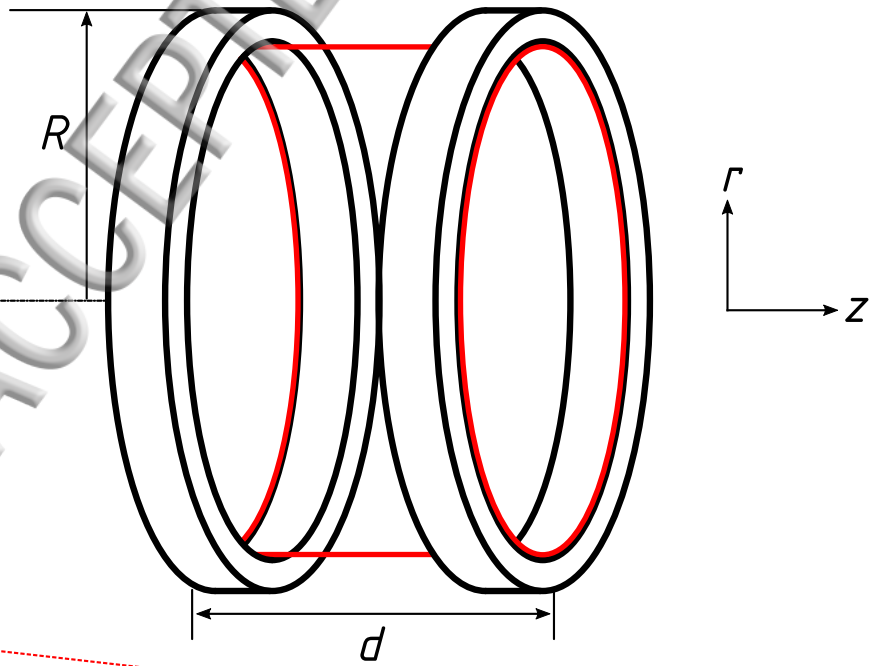

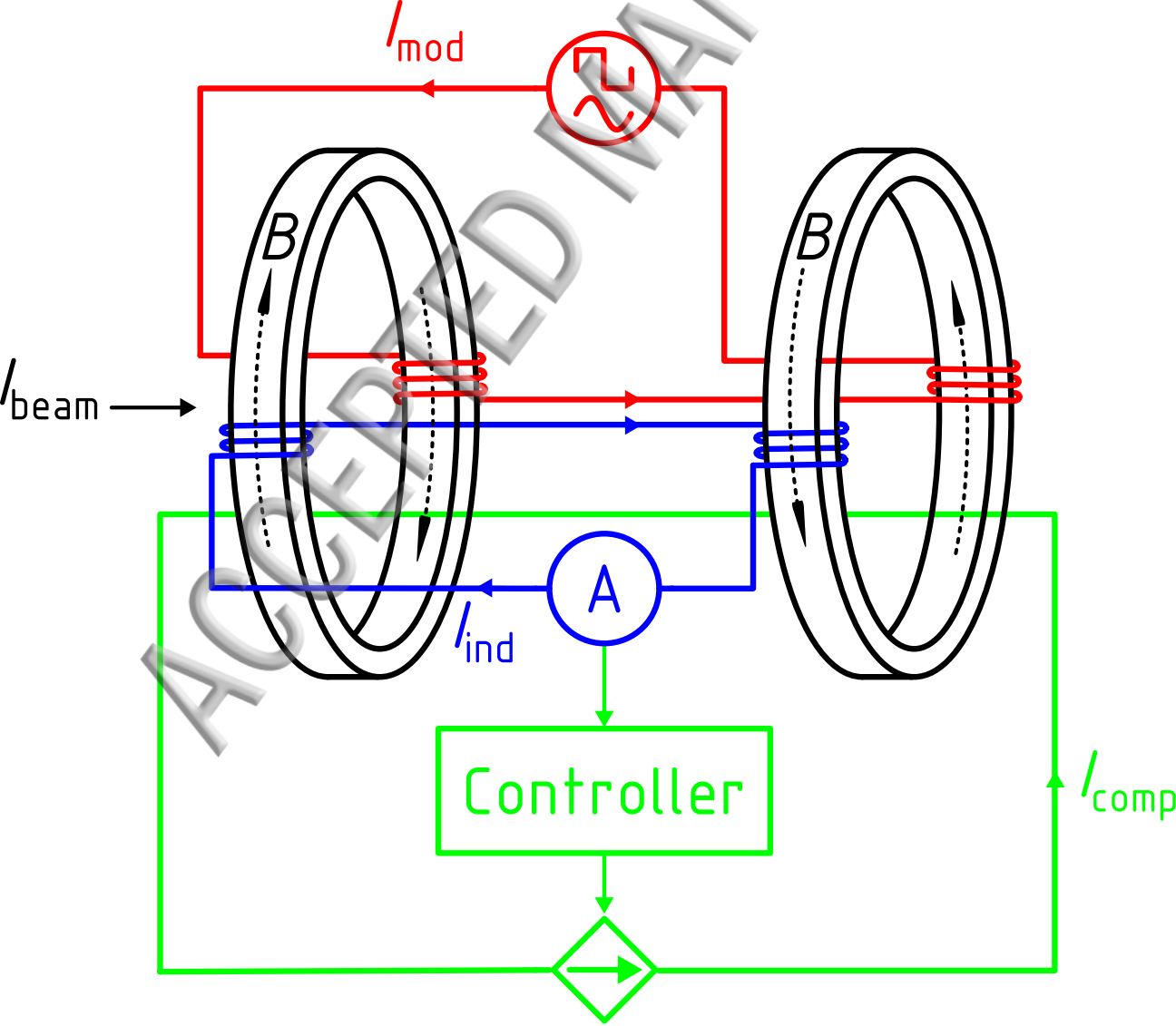

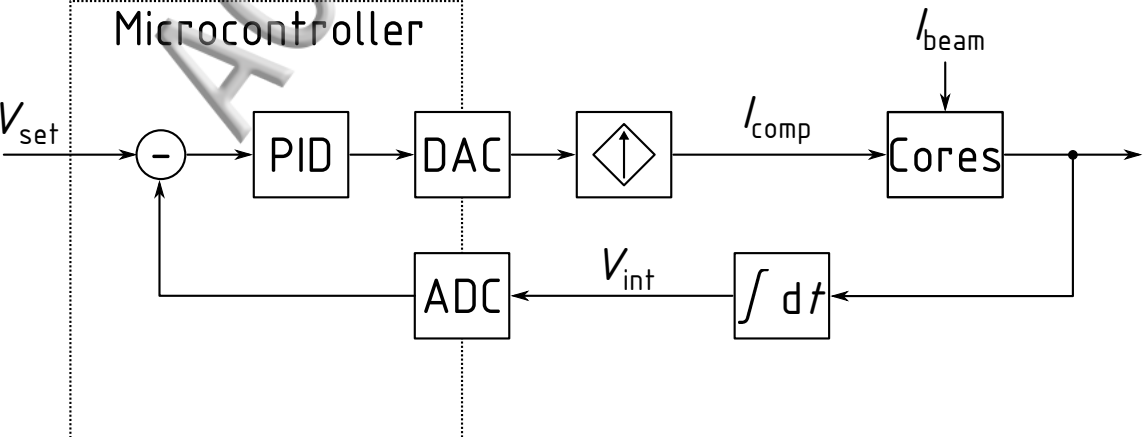
Microcontroller
V_{set}
PID
DAC
I_{comp}
I_{beam}
Cores
ADC
V_{int}
$\int dt$

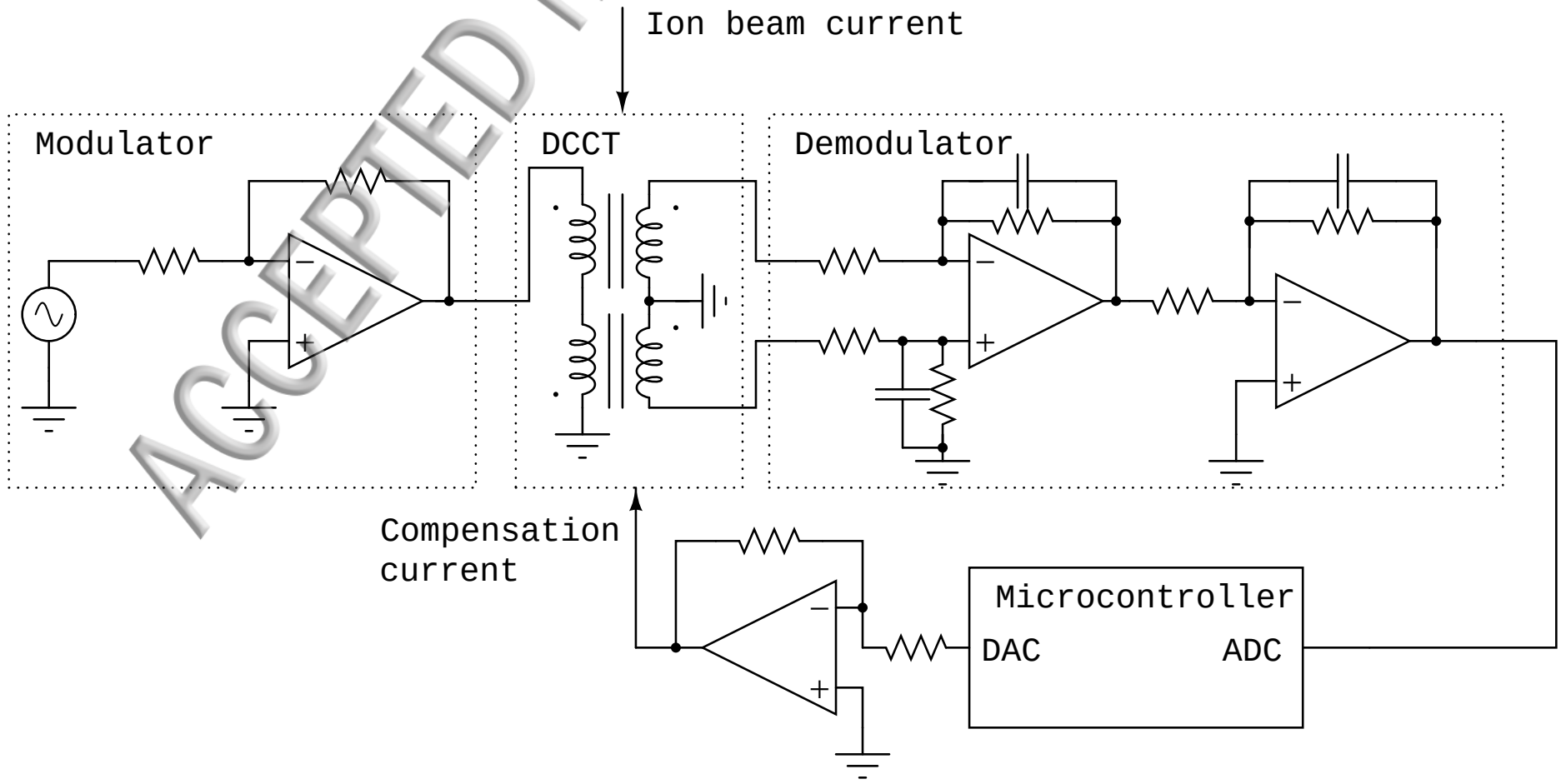
Ion beam current
Modulator
DCCT
Demodulator
Compensation current
Microcontroller
DAC
ADC

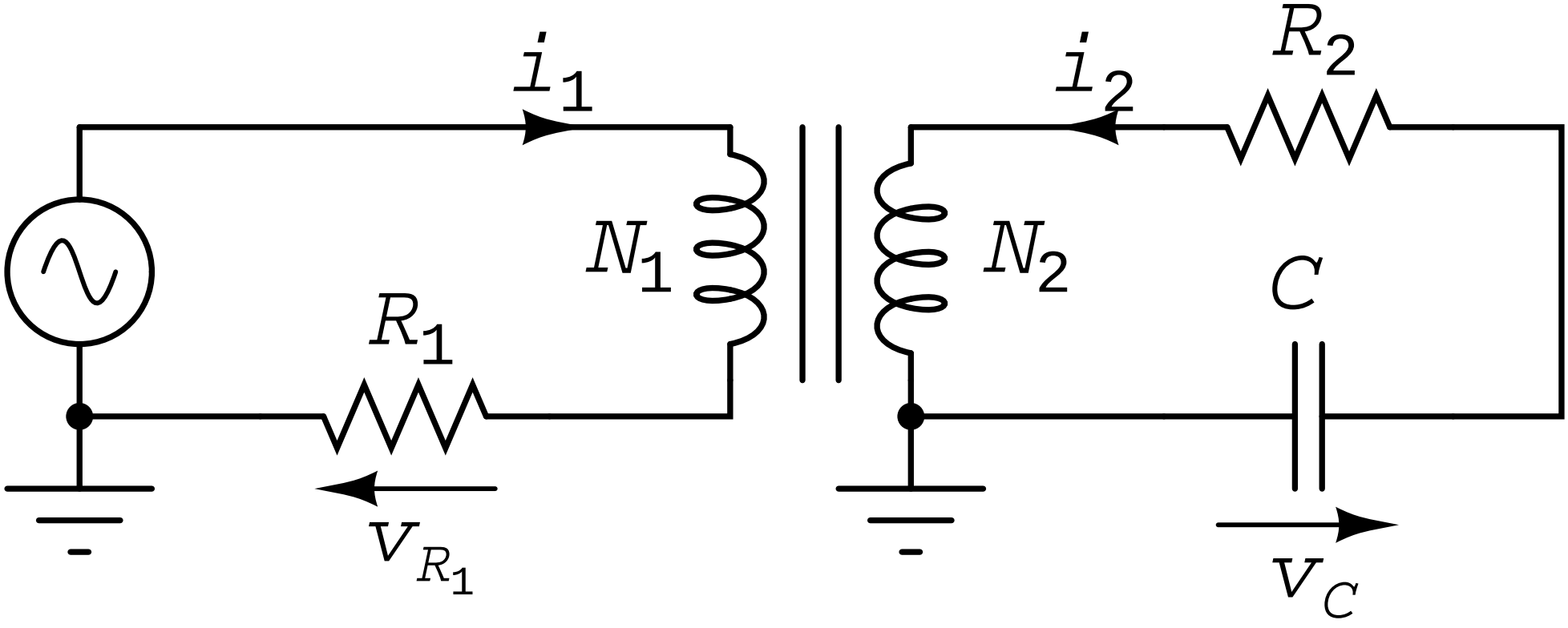
i_1
i_2
R_2
N_1
N_2
C
R_1
v_{R_1}
v_C